

Enhanced 3D spatial resolution in quantitative phase microscopy using spatially incoherent illumination

Pierre Bon,^{1,3,*} Sherazade Aknoun,^{1,2} Serge Monneret,¹
and Benoit Wattellier²

¹Aix-Marseille Université, Ecole Centrale Marseille, CNRS, Institut Fresnel, Campus de Saint-Jérôme, 13013 Marseille, France

²PHASICS SA, XTEC Bat. 404, Campus de l'Ecole Polytechnique, Route de Saclay, 91128 Palaiseau, France

³Currently at Institut Langevin, ESCPI Paris-Tech, CNRS, 1 rue Jussieu, Paris, France

*pierre.bon@fresnel.fr

Abstract: We describe the use of spatially incoherent illumination to make quantitative phase imaging of a semi-transparent sample, even out of the paraxial approximation. The image volume electromagnetic field is collected by scanning the image planes with a quadriwave lateral shearing interferometer, while the sample is spatially incoherently illuminated. In comparison to coherent quantitative phase measurements, incoherent illumination enriches the 3D collected spatial frequencies leading to 3D resolution increase (up to a factor 2). The image contrast loss introduced by the incoherent illumination is simulated and used to compensate the measurements. This restores the quantitative value of phase and intensity. Experimental contrast loss compensation and 3D resolution increase is presented using polystyrene and TiO₂ micro-beads. Our approach will be useful to make diffraction tomography reconstruction with a simplified setup.

© 2014 Optical Society of America

OCIS codes: (110.0180) Microscopy; (120.5050) Phase measurement; (110.6880) Three-dimensional image acquisition; (110.1650) Coherence imaging; (050.1960) Diffraction theory.

References and links

1. E. Cuche, P. Marquet, and C. Depeursinge, "Simultaneous amplitude-contrast and quantitative phase-contrast microscopy by numerical reconstruction of fresnel off-axis holograms," *Appl. Opt.* **38**, 6994–7001 (1999).
2. G. Popescu, L. P. Deflores, J. C. Vaughan, K. Badizadegan, H. Iwai, R. R. Dasari, and M. S. Feld, "Fourier phase microscopy for investigation of biological structures and dynamics," *Opt. Lett.* **29**, 2503–2505 (2004).
3. M. Debailleul, V. Georges, B. Simon, R. Morin, and O. Haeberlé, "High-resolution three-dimensional tomographic diffractive microscopy of transparent inorganic and biological samples," *Opt. Lett.* **34**, 79–81 (2009).
4. B. Kemper, A. Vollmer, C. E. Rommel, J. Schnekenburger, and G. von Bally, "Simplified approach for quantitative digital holographic phase contrast imaging of living cells," *J. Biomed. Opt.* **16**, 026014 (2011).
5. Y. Choi, T. D. Yang, K. J. Lee, and W. Choi, "Full-field and single-shot quantitative phase microscopy using dynamic speckle illumination," *Opt. Lett.* **36**, 2465–2467 (2011).
6. N. T. Shaked, "Quantitative phase microscopy of biological samples using a portable interferometer," *Opt. Lett.* **37**, 2016–2018 (2012).
7. B. Bhaduri, K. Tangella, and G. Popescu, "Fourier phase microscopy with white light," *Biomed. Opt. Express* **4**, 1434–1441 (2013).
8. A. Barty, K. A. Nugent, D. Paganin, and A. Roberts, "Quantitative optical phase microscopy," *Opt. Lett.* **23**, 817–819 (1998).

9. S. S. Kou, L. Waller, G. Barbastathis, and C. J. R. Sheppard, "Transport-of-intensity approach to differential interference contrast (ti-dic) microscopy for quantitative phase imaging," *Opt. Lett.* **35**, 447–449 (2010).
10. K. G. Phillips, S. L. Jacques, and O. J. T. McCarty, "Measurement of single cell refractive index, dry mass, volume, and density using a transillumination microscope," *Phys. Rev. Lett.* **109**, 118105 (2012).
11. S. Bernet, A. Jesacher, S. Fürhapter, C. Maurer, and M. Ritsch-Marte, "Quantitative imaging of complex samples by spiral phase contrast microscopy," *Opt. Express* **14**, 3792–3805 (2006).
12. Z. Wang, L. Millet, M. Mir, H. Ding, S. Unarunotai, J. Rogers, M. U. Gillette, and G. Popescu, "Spatial light interference microscopy (slim)," *Opt. Express* **19**, 1016–1026 (2011).
13. M. R. Arnison, K. G. Larkin, C. J. R. Sheppard, N. I. Smith, and C. J. Cogswell, "Linear phase imaging using differential interference contrast microscopy," *J. Microsc.* **214**, 7–12 (2004).
14. D. D. Duncan, D. G. Fischer, A. Dayton, and S. A. Prahl, "Quantitative carré differential interference contrast microscopy to assess phase and amplitude," *J. Opt. Soc. Am. A* **28**, 1297–1306 (2011).
15. P. Bon, G. Maucort, B. Wattellier, and S. Monneret, "Quadriwave lateral shearing interferometry for quantitative phase microscopy of living cells," *Opt. Express* **17**, 13080–13094 (2009).
16. I. Iglesias, "Pyramid phase microscopy," *Opt. Lett.* **36**, 3636–3638 (2011).
17. A. B. Parthasarathy, K. K. Chu, T. N. Ford, and J. Mertz, "Quantitative phase imaging using a partitioned detection aperture," *Opt. Lett.* **37**, 4062–4064 (2012).
18. M. Born and E. Wolf, *Principles of Optics* (Cambridge University, 1999), chap. 9, pp. 547–553.
19. N. Streibl, "Three-dimensional imaging by a microscope," *J. Opt. Soc. Am. A* **2**, 121–127 (1985).
20. J. Primot and N. Guérineau, "Extended hartmann test based on the pseudoguiding property of a Hartmann mask completed by a phase chessboard," *Appl. Opt.* **39**, 5715–5720 (2000).
21. P. Bon, S. Monneret, and B. Wattellier, "Noniterative boundary-artifact-free wavefront reconstruction from its derivatives," *Appl. Opt.* **51**, 5698–5704 (2012).
22. P. Bon, B. Wattellier, and S. Monneret, "Modeling quantitative phase image formation under tilted illuminations," *Opt. Lett.* **37**, 1718–1720 (2012).
23. P. Bon, T. Barroca, S. Lévêque-Fort, and E. Fort, "Label-free evanescent microscopy for membrane nanotomography in living cells," *J. Biophotonics* (advance online publication, 2013).
24. V. Lauer, "New approach to optical diffraction tomography yielding a vector equation of diffraction tomography and a novel tomographic microscope," *J. Microsc.* **205**, 165–176 (2002).
25. S. S. Kou and C. J. R. Sheppard, "Imaging in digital holographic microscopy," *Opt. Express* **15**, 13640–13648 (2007).
26. T. Kim, R. Zhou, M. Mir, S. D. Babacan, P. S. Carney, L. L. Goddard, and G. Popescu, "White-light diffraction tomography of unlabelled live cells," *Nat. Photonics*, advance online publication (2014).
27. F. Montfort, T. Colomb, F. Charrière, J. Kühn, P. Marquet, E. Cuche, S. Herminjard, and C. Depeursinge, "Submicrometer optical tomography by multiple-wavelength digital holographic microscopy," *Appl. Opt.* **45**, 8209–8217 (2006).
28. S. S. Kou and C. J. R. Sheppard, "Image formation in holographic tomography: high-aperture imaging conditions," *Appl. Opt.* **48**, H168–H175 (2009).
29. R. Fiolka, K. Wicker, R. Heintzmann, and A. Stemmer, "Simplified approach to diffraction tomography in optical microscopy," *Opt. Express* **17**, 12407–12417 (2009).
30. W. J. Choi, D. I. Jeon, S.-G. Ahn, J.-H. Yoon, S. Kim, and B. H. Lee, "Full-field optical coherence microscopy for identifying live cancer cells by quantitative measurement of refractive index distribution," *Opt. Express* **18**, 23285–23295 (2010).
31. Y. Cotte, F. Toy, P. Jourdain, N. Pavillon, D. Boss, P. Magistretti, P. Marquet, and C. Depeursinge, "Marker-free phase nanoscopy," *Nat. Photonics* **7**, 113–117 (2013).
32. P. Gao, G. Pedrini, and W. Osten, "Structured illumination for resolution enhancement and autofocusing in digital holographic microscopy," *Opt. Lett.* **38**, 1328–1330 (2013).
33. S. Chowdhury and J. Izatt, "Structured illumination quantitative phase microscopy for enhanced resolution amplitude and phase imaging," *Biomed. Opt. Express* **4**, 1795–1805 (2013).
34. X. Chen, N. George, G. Agranov, C. Liu, and B. Gravelle, "Sensor modulation transfer function measurement using band-limited laser speckle," *Opt. Express* **16**, 20047–20059 (2008).
35. Y. Cotte, F. M. Toy, C. Arfire, S. S. Kou, D. Boss, I. Bergoënd, and C. Depeursinge, "Realistic 3d coherent transfer function inverse filtering of complex fields," *Biomed. Opt. Express* **2**, 2216–2230 (2011).
36. A. Tikhonov, A. Goncharsky, V. Stepanov, and A. Yagola, *Numerical Methods for the Solution of Ill-Posed Problems*, Mathematics and Its Applications (Springer, 1995).
37. N. Wiener, *Extrapolation, Interpolation, and Smoothing of Stationary Time Series* (The MIT Press, 1964).
38. Y. Sung, W. Choi, C. Fang-Yen, K. Badizadegan, R. R. Dasari, and M. S. Feld, "Optical diffraction tomography for high resolution live cell imaging," *Opt. Express* **17**, 266–277 (2009).
39. P. Bon, B. Rolly, N. Bonod, J. Wenger, B. Stout, S. Monneret and H. Rigneault, "Imaging the Gouy phase shift in photonic jets with a wavefront sensor," *Opt. Lett.* **37**, 3531–3533 (2012).
40. R. Barer, "Interference microscopy and mass determination," *Nature* **169**, 366–367 (1952).
41. S. Aknoun, P. Bon, J. Savatier, B. Wattellier, and S. Monneret, "Quantitative birefringence imaging of biological

1. Introduction

Optical microscopy has been widely used for hundred of years for bio-medical imaging. However, most of nonmodified biological samples are transparent at optical wavelengths, leading to low-contrast images when using a conventional intensity-sensitive sensor on a microscope. However, even if the sample does not absorb light, it presents a refractive index distribution that perturbs the wave front and can be used as an intrinsic source of contrast. Quantitative phase imaging (QPI) is thus a useful tool to observe biological sample. Several quantitative techniques have been developed in the past two decades and various approaches can be listed: Mach-Zender or Michelson design [1–7], transport of intensity equations [8–10], phase engineering in the pupil [11, 12], quantitative differential interference contrast [13, 14] or self-interference phenomenon [15–17].

Quantitative phase imaging is commonly used with coherent illumination because it allows a relatively simple interpretation of the measurement, but the drawback is that it also generates speckle distribution in the images. Only a few techniques can deal with a low temporal coherent source [6, 7, 9, 11, 13, 15, 17] or with a partially spatially incoherent illumination (SII) [5, 10, 15–17] without suffering from reconstruction artifacts. However, going from coherent illumination to incoherent illumination (particularly SII) is an important feature for both signal-to-noise ratio and resolution purpose. Indeed, the lateral resolution is doubled by aperture synthesis effect between coherent spatial illumination and incoherent spatial illumination. The axial-resolution gain is even higher as it has been shown in tomographic setups [3].

In this paper we propose to study quantitative phase imaging under any illumination spatial coherence using a quadriwave lateral shearing interferometer (QWLSI) [15]. We consider an approach which is valid not only within the paraxial approximation [10] but for any collection numerical aperture (NA_{coll}) and illumination numerical aperture (NA_{ill}). The approach is based on SII contrast loss determination and compensation to obtain quantitative analysis from measurements. The modulation transfer function (MTF) describes this contrast loss as a function of the object spatial frequencies. Theoretical MTF is well known in conventional intensity imaging setup [18] because it allows quantitative interpretation of the measurements. It can be generalized in 3D and also for phase-sensitive imaging setup [19]. We propose in this paper a simulation method to determine the MTF of the couple microscope / QWLSI for both intensity and optical path difference (OPD). MTF are discussed under both the projective approximation (equivalent to a 2D MTF) and the complete 3D mapping. We then compare the simulated incoherent images with experimental ones. We finally validate our approach with point-like objects and show that this technique drastically increases phase and intensity image 3D-resolution.

2. Setup for QWLSI measurements under spatially incoherent illumination

2.1. Optical setup

We use a nonmodified inverted microscope (Ti-U, Nikon, Japan) equipped with a Z-axis piezo stage (PiFoc, Physik Instrumente, Germany) to allow stack imaging and a $100\times$, $NA_{coll} = 1.3$ objective (Nikon, Japan). To generate an incoherent trans-illumination, the native halogen source of the microscope is used. The white-light is filtered using a 700 ± 30 nm band-pass filter in order to neglect both the wavelength dependency of the 2D/3D MTF and the sample dispersion.

In order to tune the illumination spatial coherence, an oil immersion condenser ($NA_{ill}=1.4$, Nikon, Japan) is used. This makes our source completely tunable regarding the spatial coherence. Indeed, by closing the aperture diaphragm, the illumination numerical aperture $NA_{ill} \rightarrow 0$

and thus the illumination is close to a collimated plane-wave (*i.e.* a spatially coherent illumination). On the opposite, by opening the aperture diaphragm, the illumination numerical aperture can be set to $NA_{ill} = NA_{coll} = 1.3$, *i.e.* a so-called fully SII [18]. Figure 1 shows the setup scheme.

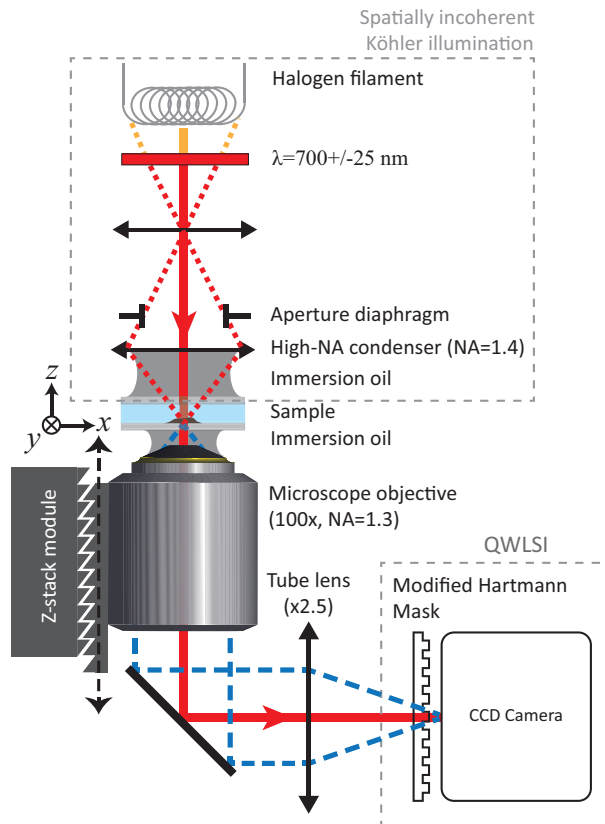


Fig. 1. Schematic of the optical setup used in this paper.

The sample is imaged onto a commercial QWLSI (SID4Bio, Phasics, France), composed of a Modified Hartmann Mask (MHM [20]) and a CCD camera. A tube lens $\times 2.5$ is used in order both to perfectly sample the images (Nyquist criterion) and to have a well contrasted QWLSI interferogram even when the illumination numerical aperture is equal to the collection one (*i.e.* Full spatially incoherent illumination). A further discussion about this point is made in the following section.

2.2. Quantitative phase imaging under incoherent illumination

In this part, we propose to discuss what can be extracted from a QWLSI interferogram under coherent plane-wave illumination and what is obtained when the same algorithm is applied to an incoherent superposition of interferograms.

Under a plane wave illumination, QWLSI allows to retrieve both the electromagnetic (EM) field intensity and its OPD gradients along two orthogonal image-space directions x and y . After numerical integration, the OPD is retrieved in a quantitative way [21].

More precisely, in the scope of phase imaging with a plane-wave illumination, the OPD can be described as follows [22]:

$$OPD \approx \int_{sample} \Delta n \times \frac{dz}{\cos\left(\left|\vec{\theta}_{ill}\right|\right)}, \quad (1)$$

where Δn is the local refractive index difference between the sample and the surrounding medium, $\vec{\theta}_{ill}$ the illumination angle and z the optical axis. For sake of simplicity and readability, we develop our next reasoning in one transverse dimension x , as the extension to two transverse dimensions is straightforward. Under a plane-wave electromagnetic (EM) field $\sqrt{I} \cdot e^{\frac{2j\pi}{\lambda} \cdot OPD} \cdot e^{2j\pi \cdot \text{Tilt}}$ of wavelength λ , the interferogram i generated by a QWLSI on a sensor can be written, in one dimension, as follows :

$$i\left(\vec{\theta}_{ill}, x, z\right) \approx I\left(\vec{\theta}_{ill}, x, z\right) \left[1 + \cos\left(\frac{2\pi}{\Lambda} \left[x - z_p \frac{\partial OPD}{\partial x}\left(\vec{\theta}_{ill}, x, z\right) - z_p \cdot \tau\left(\vec{\theta}_{ill}\right)\right]\right)\right], \quad (2)$$

where I is the EM field intensity, Λ is the diffraction grating period, z_p the distance between the diffraction grating and the sensor, τ the wavefront tilt component due to the illumination angle at the sensor level (see Eq. (5)) and z the position of the sensor along the optical axis. Let us note $\alpha = 2\pi z_p / \Lambda$ the calibration lever arm. By demodulating around the 0^{th} order spatial frequency and around the Λ spatial frequency, one can extract respectively I and the OPD gradient along x by considering :

$$\left\{ \begin{array}{l} I = \text{FT}^{-1} [\text{FT}[i] \otimes \delta(k)] \\ \frac{\partial OPD}{\partial x} = \frac{1}{\alpha} \text{Arg} \left\{ \text{FT}^{-1} [\text{FT}[i] \otimes \delta\left(k - \frac{\Lambda}{2\pi}\right)] \right\} \end{array} \right. , \quad (3)$$

where δ is the Dirac distribution, Arg the complex argument function, FT the Fourier transform and FT^{-1} the inverse Fourier transform. Please note that to obtain individual images for intensity and OPD gradients, a low-pass filtering is also applied by Fourier space clipping around $k = 0$ and $k = \Lambda/2\pi$.

Considering now an incoherent illumination, the obtained interferogram i_{SI} with QWLSI is equal to the sum of each unit interferogram formed by each source point :

$$i_{SI}(x, z) = \int_{\vec{\theta}_{ill}} i\left(\vec{\theta}_{ill}, x, z\right) d\vec{\theta}_{ill}. \quad (4)$$

It is well known that wave front dividing interferometers (such as QWLSI) suffer from interferogram blur when the source is not a point. Indeed, as each unit interferogram has a different tilt value, it is laterally shifted on the sensor with respect to the others. This tilt component at the QWLSI level can be written [15]:

$$\tau\left(\vec{\theta}_{ill}\right) = \frac{\tan\left(\left|\vec{\theta}_{ill}\right|\right)}{M}, \quad (5)$$

where M is the microscope magnification. Using high lateral magnification between the object and the image space leads to a huge reduction of the angular dispersion in the image space. So, even for totally incoherent illumination in the object plane, it is possible to obtain a well contrasted interferogram by using a high-magnification between the object and the QWLSI plane [15]. As an example, Fig. 2 shows interferograms obtained by imaging at $250\times$ magnification [15]. As an example, Fig. 2 shows interferograms obtained by imaging at $250\times$ magnification [15]. In Fig. 2(a), a spatially coherent source (halogen source and Köhler aperture diaphragm closed to the minimum) has been used, whereas spatially incoherent source (halogen source and Köhler aperture diaphragm opened to reach $\text{NA}_{illum} = \text{NA}_{coll} = 1.3$) has been used in Fig. 2(b).

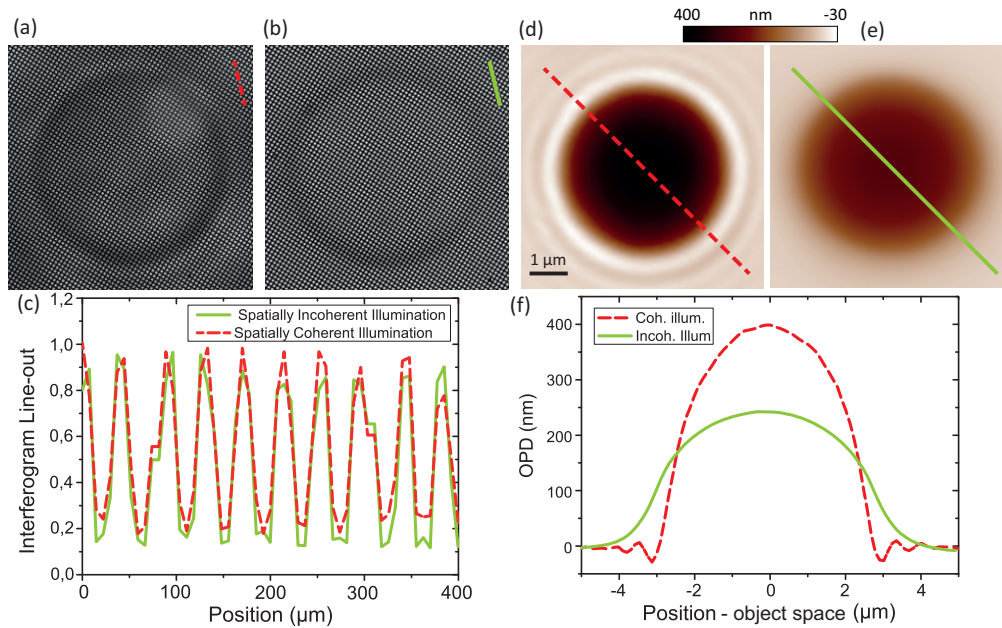


Fig. 2. 5 μm polystyrene microbead immersed in a $n = 1.556$ medium, imaged at $250\times$, $\text{NA}_{\text{coll}} = 1.3$. (a) QWLSI interferogram with $\text{NA}_{\text{illum}} \approx 0.08$. (b) QWLSI interferogram with $\text{NA}_{\text{illum}} = 1.3$. (c) Profile plots of (a) (dashed red line) and (b) (solid black line). (d) OPD image retrieved from (a). (e) OPD image retrieved from (b). (f) Profile plots of (d) (dashed red line) and (e) (solid black line).

The interferogram contrast is close to unity for both coherent and incoherent illuminations (Fig. 2(c)). Local contrast analysis gives an average fringe contrast of 0.88 for the coherent illumination (theoretical value = 1) and of 0.85 for the incoherent illumination (theoretically 0.89 as calculated using [15]).

Although perfectly well contrasted, the interferograms under coherent illumination and SII analyzed with the same algorithm (*i.e.* demodulation according to Eq. (3) and gradient integration [21]) lead to different OPD results. This is perfectly visible on Figs. 2(d) and 2(f): SII imaging leads to a decrease in the OPD ($OPD_{\text{SII}}^{\text{max}} = 0.6 \cdot OPD_{\text{coh}}^{\text{max}}$); this effect will be discussed in the part 3.3.

To sum up, SII induces thus two different effects: fringe blurring and OPD amplitude reduction. In our case, we demonstrated that the OPD amplitude reduction is the dominant effect. Moreover, please note that the SII intensity and OPD fields are not rigorously the phase and the intensity of an existing EM field as these notions are dedicated to coherent fields.

3. Effect of the illumination coherence on the image formation

3.1. Scalar model and effect of polarization

In this paper we propose an EM field scalar description that neglects any polarization effect. As we work with non-polarized illumination / detection and with sub-critical angles only [23], this assumption is valid in first approach for this entire paper. Polarization effect may affect the model at second order and explain some residual mismatches between the theoretical model and the experiment.

Moreover, for studies with polarized light at high-numerical aperture or if the objective nu-

merical aperture is higher than the medium refractive index (*i.e.* evanescent wave are collected), a vector approach will be necessary to take into account the influence of polarization on the microscope optical response. However, these kind of studies are beyond the scope of this paper.

3.2. Resolution improvement

The image formation on a sensor is directly related to the questions of both lateral and axial resolution (also known as sectioning). In the context of scattering microscopy, the lateral resolution is well known and described for more than hundred of years. According to Abbe's formula, the lateral unpolarized resolution r_{xy} of a perfect microscope is equal to:

$$r_{xy} = \frac{\lambda_0}{\text{NA}_{ill} + \text{NA}_{coll}}, \quad (6)$$

where λ_0 is the free-space wavelength of the light, NA_{ill} is the numerical aperture of the illumination and NA_{coll} is the numerical aperture on the collection (*i.e.* the objective numerical aperture). From this equation, one can notice that, for a given microscope objective, both the wavelength and the angular content of the illumination contribute to the lateral resolution. It has to be noticed that for unpolarized fluorescence imaging, where the image is formed by the incoherent re-emission of light, the same formula is used considering that $\text{NA}_{ill} = \text{NA}_{coll}$.

The coherence of the illumination beam is thus a key point in scattering imaging. Indeed, as the scattered EM field is completely related with the incident EM field, it is essential to know the illumination scheme. It is convenient to consider any incoherent illumination as the superposition of coherent plane-waves. In the case of semi-transparent object imaging, the interaction between the object and the coherent light can be described as follows :

$$\vec{k}_d = \vec{k}_i + \vec{K}_o, \quad (7)$$

where \vec{k}_i is the wave-vector of the incident plane wave, \vec{k}_d is a diffracted wave-vector and \vec{K}_o is an object 3D spatial frequency. As the scattering is an elastic process, $\|\vec{k}_i\| = \|\vec{k}_d\|$ and:

$$k_i^2 = (k_{ix} + K_{ox})^2 + (k_{iy} + K_{oy})^2 + (k_{iz} + K_{oz})^2. \quad (8)$$

So the locus of the accessible object frequencies is a sphere of center (k_{ix}, k_{iy}, k_{iz}) and of radius k_i . This sphere is called the Ewald sphere [24, 25] and is well known in the scope of crystallography. The accessible object frequencies can be decomposed in two solutions:

$$\begin{cases} K_{oz} = -k_{iz} + \sqrt{k_{iz}^2 - (K_{ox}^2 + K_{oy}^2 + 2 \cdot K_{ox} \cdot k_{ix} + 2 \cdot K_{oy} \cdot k_{iy})} & [1] \\ K_{oz} = -k_{iz} - \sqrt{k_{iz}^2 - (K_{ox}^2 + K_{oy}^2 + 2 \cdot K_{ox} \cdot k_{ix} + 2 \cdot K_{oy} \cdot k_{iy})} & [2] \end{cases} \quad (9)$$

The solution 1 corresponds to the accessible object frequencies when the illumination/detection scheme is in transmission (*i.e.* trans-illumination scheme) and the solution 2 corresponds to the frequencies when the illumination/detection is in reflection. For the remaining of this paper, the case of trans-illumination only will be considered. Figure 3(a) presents an example of the measurable object frequencies in trans-illumination, in the case of an illumination plane-wave propagating along the (K_{oz}) axis. Due to the collection numerical aperture, the spatial object frequencies that can be retrieved from each spatially coherent illumination is thus a fraction of the Ewald sphere. An example of accessible object frequencies with trans-illumination and plane-wave illumination is presented in Fig. 3(b), considering an immersion objective (immersion refractive index n_{imm} , $\text{NA}_{coll} = 0.75\lambda_m/\lambda_0$, with $\lambda_m = \lambda_0/n_{imm}$).

Considering now an incoherent illumination and again a trans-illumination scheme, the accessible object frequencies are the union of all the Ewald sphere portions accessible by each

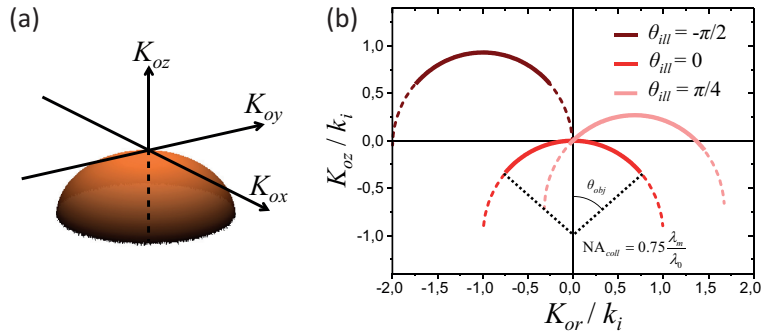


Fig. 3. Measurable object frequencies in trans-illumination when illuminated by a plane wave propagating: (a) along the (K_{oz}) axis. (b) along the optical axis (red curve), with an angle respect to the optical axis off $\pi/4$ (pink curve) and with an angle of $-\pi/2$ (brown). The dashed dot regions indicate the frequencies filtrated by the collection microscope objective of numerical aperture $NA_{coll} = 0.75 \frac{\lambda_m}{\lambda_0}$.

unit plane wave constituting the incoherent source decomposition. The object frequency support can thus be greatly improved compared with coherent illumination. At this point polychromatic incoherent source (ex. white LED) and spatially incoherent source (ex. wavelength filtered halogen, such as in this paper) have to be considered separately.

Polychromatic incoherent illumination

Figure 4(a) shows the accessible object frequencies for a polychromatic source with a maximum wavelength equal to $2 \times$ the minimum wavelength (equivalent to a visible light spectrum); the average wavelength is called $\langle \lambda \rangle$ and its associated wave-vector $\langle k_i \rangle$. The numerical aperture is the same as the one in Fig. 3(b): $NA_{coll} = 0.75 \lambda_m / \lambda_0$.

In trans-illumination, the lateral resolution of polychromatic imaging is the one given by the shortest wavelength of the spectrum: thus, there is no real gain in lateral resolution. However, the 3D accessible object frequencies (in green in Fig. 4(a)) are extended compared with monochromatic imaging: the diffraction rings observed in coherent images are reduced which slightly improves the image quality [26]. The axial resolution is also improved in trans-illumination but the effect is much more important in reflection [25] allowing, for example in conventional diffraction tomography, an approximated tomographic reconstruction [27].

Spatially incoherent illumination, SII

Figure 4(b) shows the support of accessible object frequencies considering a fully SI illumination [18] of numerical aperture $NA_{ill} = NA_{coll}$ and of wavelength $\langle \lambda \rangle$.

The frequency support under incoherent illumination is the same as the one obtained in diffraction tomography, where a series of coherent illumination are sent on the sample and numerically combined [3, 25, 28].

SI illumination allows a much more interesting gain in trans-illumination compared to polychromatic incoherent illumination. The lateral resolution can be doubled compared to the coherent illumination when the illumination numerical aperture is equal to the collection numerical aperture (Eq. (6) and Fig. 4(b) in green). This is the so-called aperture synthesis effect. The axial resolution is also increased, leading to axial sectioning. It has been widely used, for example, in conventional diffraction tomography [3, 24, 29–31]. The axial sectioning can be understood as follows. Each unit illumination is spreading the out-of-focus volume along a specific and given direction: the consequence with SII is a blurred information for out-of-focus planes. In

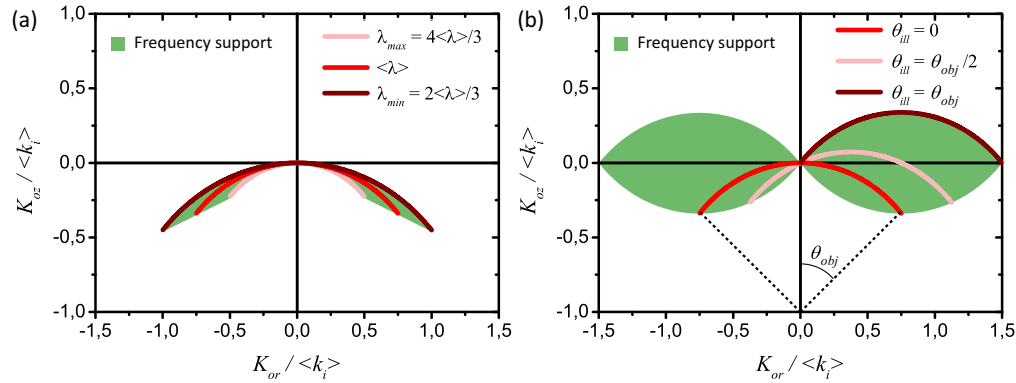


Fig. 4. Measurable object frequencies with an objective of $NA_{coll} = 0.75\lambda_m/\lambda_0$, trans-illuminated by a incoherent source. (a) Polychromatic spatially coherent illumination with $\lambda_{max} = 2\lambda_{min}$. In pink: coherent contribution at $\lambda_m = \lambda_{max}$, in red: at $\lambda_m = \langle\lambda\rangle$, in brown: at $\lambda_m = \lambda_{min}$. In green: complete accessible frequencies. (b) Monochromatic ($\lambda_m = \langle\lambda\rangle$) spatially incoherent illumination with $NA_{ill} = NA_{coll}$. In red: coherent contribution at $\theta_{ill} = 0$, in pink: at $\theta_{ill} = \theta_{obj}/2$, in brown: at $\theta_{ill} = \theta_{obj}$. In green: complete accessible frequencies.

the same time the in-focus plane does not spread for any unit illumination. This explains the local high contrast and out-of-focus rejection obtained on the SII image.

The accessible frequencies under SII form the so-called peanut-shaped structure, where the frequencies along the optical axis can not be reconstructed (the *missing apple core* [3]). It is interesting to mention here that under fully SI illumination (when the illumination numerical aperture is equal to the collection numerical aperture) the lateral resolution is theoretically the same as the one obtained using structured illumination holography [32, 33]. Moreover, the 3D resolution in fully SI trans-illumination scheme is the same as the resolution in conventional fluorescence imaging.

In trans-illumination, which is the scheme used in this paper, the gain compared to plane-wave illumination is thus much more important when considering SI illumination rather than a polychromatic incoherent illumination. This is why we only will consider quasi-monochromatic SI illumination below.

3.3. Modulation transfer function (MTF) and deconvolution

The major problem that emerges when using incoherent illumination, is an image contrast loss at the object highest spatial frequencies that prevents most of the image quantitative interpretations. As an example, the zero frequency (0,0,0) is accessible with any illumination angle within the collection numerical aperture. On the opposite, each frequency with the maximum lateral K_{or} is only accessible with a single maximum angle collected by the objective. More generally, the number of possible angles depends on the spatial frequency, implying there is no bijection between the spatial frequencies and the illumination angles. The lower the object spatial frequency is, the higher the number of illumination angles that are able to diffract on it. Thus, the amount of energy is higher for the lower spatial frequencies explaining the loss of contrast at high spatial frequencies.

This loss of contrast is characterized by the so-called Modulation Transfer Function (MTF) [18]. We will consider that our optical system is perfect (no optical aberration) so its MTF is the one of perfect optics with flat circular aperture stop. The sensor can also modify the MTF and needs to be taken into account in the general case [34]. For two dimensional objects

and intensity measurements (ex. daily life scene observed with a camera), the MTF is well defined [18]. However for high (NA_{coll}, NA_{ill}) optical systems, non-intensity sensitive sensor (ex. quantitative phase imaging, QPI) and/or when 3D imaging of semi-transparent sample is considered, the MTF is more complex to describe. Streibl described a theoretical 3D MTF in intensity and phase but using the first Born and paraxial approximations [19]. More recently [35], Cotte *et al.* proposed a way to measure coherent transfer function for QPI using nano-holes and an holographic microscope in order to take into account the optical aberrations, but this approach is limited to coherent illumination. In this paper, we propose a way to determine MTF for either intensity or phase using image simulation tools [22], taking into account the response of our QWLSI sensor.

Regularization and deconvolution

As mentioned, contrast loss compensation is important for quantitative imaging. Under the hypothesis of perfect optical system, the MTF is constant over the whole field of view. A way to deconvolve the images knowing the MTF is to work in the Fourier space. In this case:

$$\tilde{I}_{Deconv} = \frac{\tilde{I}}{MTF}, \quad (10)$$

where \tilde{I} and \tilde{I}_{Deconv} are the Fourier transform of respectively the image and the deconvolved image. As the MTF usually contains zeros (*i.e.* frequencies non-transmitted by the optical system) a brutal deconvolution multiplying the image in the Fourier space by $1/MTF$ leads to large noise amplification. Regularization methods can be used to limit this effect: the general idea is to substitute the function $1/MTF$ by $1/MTF_{reg}$ which presents the following properties:

$$\begin{cases} \frac{1}{MTF_{reg}} \rightarrow 1 \text{ when } MTF \rightarrow 0 \\ \frac{1}{MTF_{reg}} \rightarrow \frac{1}{MTF} \text{ else} \end{cases}. \quad (11)$$

The key point is to determine when the MTF is considered to tend to 0. We can cite for example the Tikhonov regularization [36] where an empirical constant fixes the MTF limit, or the Wiener regularization [37] which is more efficient as it also takes into account the signal-to-noise ratio (SNR) at each frequency ν :

$$\frac{1}{MTF_{reg}^{Wiener}}(\nu) = \frac{1}{MTF(\nu)} \cdot \left[\frac{|MTF(\nu)|^2}{|MTF(\nu)|^2 + \frac{1}{SNR(\nu)}} \right]. \quad (12)$$

In this paper, we will apply Wiener regularization in each deconvolution process. Let us now discuss a way to determine the MTF.

4. Modulation transfer function determination by simulation tools

As explained in the section 3.3, the main drawback of using incoherent illumination is the contrast loss which occurs both for the intensity and the OPD. This contrast loss originates jointly from the imaging device (microscope) and the detection device (QWLSI). In order to interpret the measurements, we need to compensate for the contrast loss of OPD and intensity.

We propose now a way to determine the MTF using simulation tools applied to a set of intensity and OPD images obtained with a well-chosen radial target under arbitrary illumination spatial coherence.

4.1. Generalized product of convolution for simulation of SI images

The generalized product of convolution (G-POC) is used to simulate the image formation (OPD and intensity) of any sample illuminated by a tilted collimated plane-wave, under the simple diffraction approximation [22]. This algorithm is intrinsically able to deal with thick samples as it takes into account the defocus component for each object slice: this is especially useful for 3D MTF determination.

As a SII can be considered as the incoherent superposition of coherent plane-waves, it is possible to simulate the image formation under SII by the sum of coherent EM fields obtained in the image plane. We thus use the G-POC by varying the illumination angle in order to generate a whole set of such unit EM fields. Each EM field is used to create an interferogram according to Eq. (2). The interferograms are next summed and analyzed with the QWLSI standard algorithm to obtain the SII OPD and intensity fields.

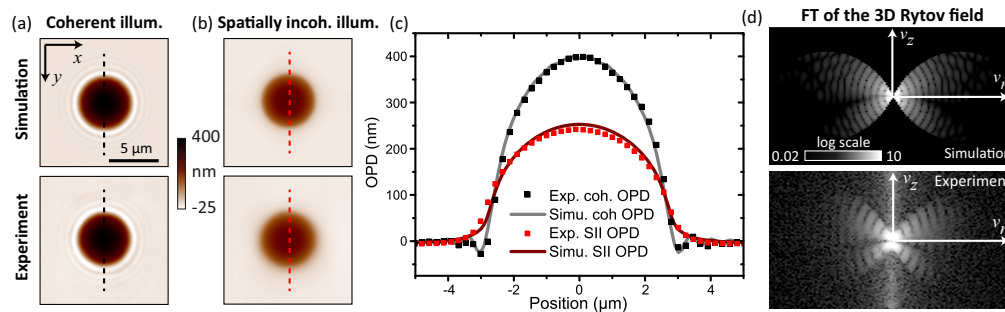


Fig. 5. (a) OPD images under coherent illumination of a $5 \mu\text{m}$ polystyrene bead immersed in $n_{\text{med}} = 1.542$ with the setup described in the part 2.1. Top: Simulated image using G-POC. Bottom: Experimental image. (b) Same as (a) but with SI illumination. (c) Profile plots of the OPD images. Black dots: experiment with coherent illumination (a,top). Gray line: simulation (a,bottom). Red dots: experiment with SII (a,top). Burgundy line: simulation (a,bottom). (d) Fourier transform (logarithmic scale) of the 3D Rytov EM field. Top: Simulation using G-POC. Bottom: Experiment.

Figure 5 shows the accuracy of the simulation against the experiment under coherent (Fig. 5(a)) and SI illumination (Fig. 5(b)), as confirmed by the line-outs of Fig. 5(c). The simulation of intensity and OPD images under SII is possible by varying the focus and Fig. 5(d) shows a comparison in the Fourier space between simulation with G-POC and experiment of the 3D Rytov field (see part 4.3). The 4 lobes-shapes are very similar.

G-POC allows to accurately simulate the image formation under SII and is used in next sections to calculate the MTF from the OPD images obtained with well-chosen model samples.

4.2. Projective modulation transfer function

Although semi-transparent microscopic samples are in general 3D structures, 2D measurements of OPD and intensity under SII can be of interest. In particular when the so-called projective approximation [15] is valid as for thin (*i.e.* thinner than the SI axial resolution) or weakly scattering samples for example. In that cases, proper determination of a two dimensional MTF in both intensity and OPD leads to reach quantitative measurements.

To simulate the contrast loss due to incoherent field detection with a QWLSI, let us consider the following 2D parametric object defined by its complex refractive index distribution:

$$\Delta n(r, \psi) = \Delta n_0 \cos(\psi \cdot N), \quad (13)$$

where (r, ψ) are the polar coordinates, Δn_0 a complex refractive index value, N is an arbitrary integer. This kind of object is known as a radial target and is commonly used for 2D intensity MTF measurements of imaging systems. Indeed, it contains all lateral frequencies v_r (at one r corresponds one v_r). It can be used as a phase object (for MTF_{OPD} determination) by using a pure real Δn_0 , or as an intensity object (for $\text{MTF}_{\text{Intensity}}$ determination) with a pure imaginary Δn_0 . For MTF_{OPD} , the projective theoretical OPD modulation amplitude of such an object is $\text{OPD}_{\text{proj}} = \text{Re}[\Delta n_0] \cdot t$ where t is the object thickness which is fixed to a value as long as the projective hypothesis is valid. In the practical case, this value is chosen to be smaller than the axial resolution.

Figure 6(d) shows a simulated SII OPD image of a given radial target ($N = 60$, $\Delta n_0 = 0.02$, Fig. 6(a)) with $\text{NA}_{\text{coll}} = \text{NA}_{\text{ill}} = 1.3$. This image has been obtained using a numerical combination of imaged coherent EM fields under different illumination angles, as described in the previous section. Compared to the OPD image obtained with a plane-wave illumination along the optical axis (Fig. 6(b)), both the resolution improvement and the contrast loss are visible in the center of the images. As a comparison, Fig. 6(c) shows the image obtained with a plane-wave illumination at the maximum illumination angle along the x axis: although higher frequencies are visible, the image looks clearly different from the object avoiding any direct interpretation.

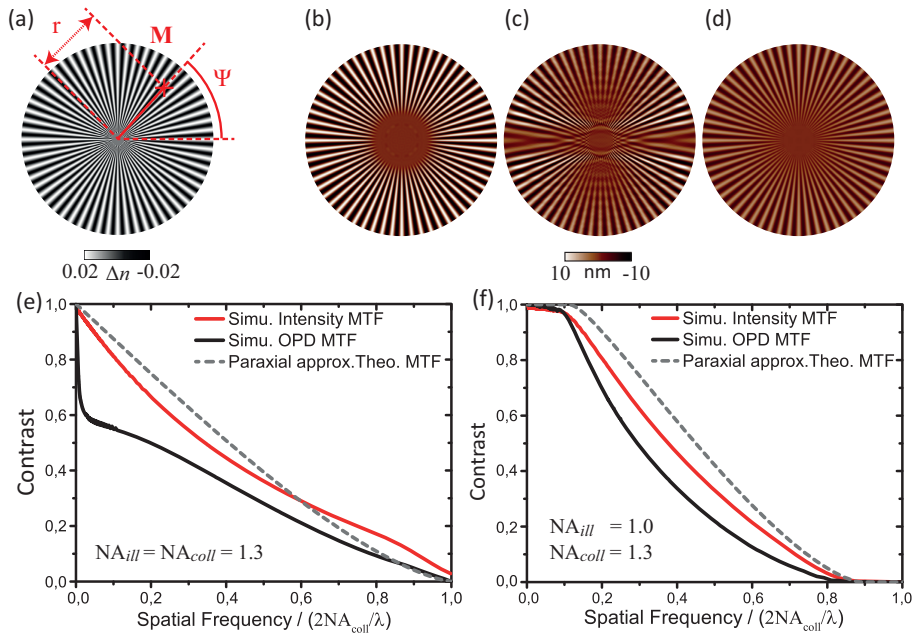


Fig. 6. (a) 2D radial target ($N = 60$ and $\Delta n_0 = 0.02$). (b) Simulated coherent OPD simulated from the object (a) with a plane-wave illumination along the optical axis. (c) Same as (b) with the maximum illumination angle $\theta_{x,\text{ill}} = \text{asin}(\text{NA}_{\text{ill}}/n_{\text{im}})$. (d) Simulated SII OPD obtained from the object (a) with $\text{NA}_{\text{coll}} = \text{NA}_{\text{ill}} = 1.3$. (e) MTF with $\text{NA}_{\text{coll}} = \text{NA}_{\text{ill}} = 1.3$. In red: projective MTF for the intensity obtained from the simulation. In black: projective MTF for the OPD obtained from the simulation. In dashed gray: Theoretical MTF under paraxial approximation. (f) Same as (e) with $\text{NA}_{\text{coll}} = 1.3$ and $\text{NA}_{\text{ill}} = 1.0$.

To extract the OPD MTF from the simulated SII OPD and intensity images, the sinusoidal modulation is measured at different radii and is normalized by the theoretical projective OPD. The same approach is used for the intensity, using a purely imaginary Δn_0 . Figure 6(e) shows

the resulting MTFs for the intensity (in red) and the OPD (in black), considering that $NA_{coll} = NA_{ill} = 1.3$. A set of different radial targets has been used to cover the required extended range of spatial frequencies ($N=4, 8, 60$). The theoretical MTF under paraxial approximation [18] is also presented in dashed gray. The intensity MTF is close to the paraxial approximated one but the OPD MTF strongly differs with a fast decay at low frequencies. This effect is less visible for slightly different experimental conditions where $NA_{coll} = 1.3$ and $NA_{ill} = 1.0$: in that case, shown on Fig. 6(f), the OPD MTF is much closer to the paraxial one, indicating a better contrast especially at low spatial frequencies. It is thus interesting to consider a quasi-fully SII rather than a fully SII to limit the contrast loss still offering a good lateral resolution. However, projective MTFs significantly vary with numerical apertures implying simulations need to be performed for each objective/condenser NA combination.

4.3. 3D modulation transfer function

We have just seen how to determine the MTF when under the projective approximation. This function is valid only in the plane conjugated with the thin object. For thicker objects or if we want the reconstruct the 3D structure of an object, this approach is not valid any more. The 3D MTF and a stack of images acquired under SII have to be considered to extract quantitative information from measurements.

First of all, it is essential to define the theoretical OPD in 3D as the definition is not conventional. One way to define this reference OPD is to follow the approach used in diffraction tomography (DT) where a combination of EM fields acquired under various illumination angles is used [3, 38]. Each coherent EM field acquired in one plane under one illumination angle is added to the others in the Fourier space by placing the carried lateral frequencies on the Ewald sphere corresponding to its illumination angle. From this mathematical 3D complex field, it is possible to extract its phase component. Thus, one way to define the theoretical 3D OPD field (OPD_{DT}^{3D}) using the diffraction tomography formalism in the Fourier space is:

$$\widetilde{OPD}_{DT}^{3D}(K_{ox}, K_{oy}, K_{oz}) \cdot \frac{2\pi}{\lambda} = \text{Re} \left(\int_{\vec{\theta}_i} \left[\widetilde{E}_{Rytov}^i(k_{dx}, k_{dy}; z=0) \otimes \delta \left(\left\| \vec{k}_d \right\|^2 - \left\| \vec{k}_i \right\|^2 \right) \right] \cdot \frac{jk_{dz}}{\pi} d\vec{\theta}_i \right), \quad (14)$$

where \vec{K}_o , \vec{k}_i and \vec{k}_d are respectively the object vectors, illumination wave-vectors and diffracted wave-vectors as defined in the part 3.2. $\text{Re}()$ represents the real part operator, $E_{Rytov}^i = \ln(A_i e^{j \cdot 2\pi \cdot OPD_i / \lambda})$ is the so-called Rytov EM field, A_i and OPD_i are the amplitude and the OPD measured under the illumination angle $\vec{\theta}_i$. δ is the Dirac distribution. This last (and its content under brackets) is an other way to describe of the Ewald sphere. The resulting 3D OPD can be physically interpreted as the OPD accumulated during the propagation through the depth-of-field.

To simulate the contrast loss under SII, we consider now the following 3D parametric object:

$$\Delta n(r, \psi, z) = \Delta n_0 \cos(\psi \cdot N) e^{j2\pi v_{z0} z}, \quad (15)$$

where (r, ψ, z) are the cylindrical coordinates, Δn_0 a complex refractive index value, N an integer and v_{z0} the axial period of the object. This thick object is a 3D generalization of the radial target described in Eq. (13). As before, it contains all lateral frequencies v_r (at one r corresponds one v_r) but only one axial frequency v_{z0} .

To obtain the requested 3D MTF, we first simulate the SII OPD image for a given axial frequency v_{z0} (ex. in Fig. 7(a-left) for a SII OPD). Then a 3D MTF section ($v_r, v_z = v_{z0}$) is deduced by dividing the SII OPD modulation value by its theoretical one obtained after inverse

Fourier transform of Eq. (14). The procedure is repeated for different v_{z0} to finally retrieve the complete 3D MTF (Fig. 7(b) in logarithmic scale). The same approach as presented in the previous section 4.2 is used to estimate its modulation amplitude.

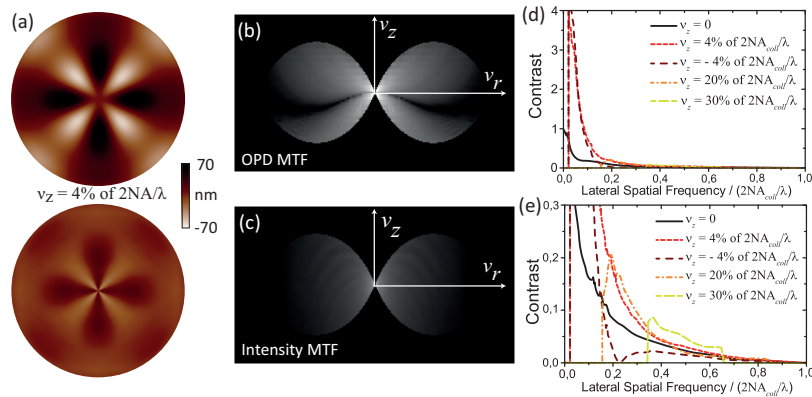


Fig. 7. (a) Imaged of a 3D radial target ($N = 4$, $v_z = 4\%$ of $2NA/\lambda$) observed in the $z = 0$ plane. Top: simulated SII OPD. Bottom: simulated Rytov combined coherent EM fields. The contrast enhancement compared to the Rytov fields is visible on the SII OPD. (b) 3D OPD MTF visualized in the (v_r, v_z) plane (logarithmic scale) considering $NA_{coll} = NA_{ill} = 1.3$. (c) Same as (b) for the 3D intensity MTF. (d) Profile plots from (c), modulation amplitude as a function of the lateral frequency normalized at $2NA_{coll}/\lambda$. Black: $v_z = 0$. Short dashed red: $v_z = 4\%$ of $2NA_{coll}/\lambda$. Medium dashed brown: $v_z = -4\%$. Dashed dot orange: $v_z = 20\%$. Large dashed yellow: $v_z = 30\%$. (e) Zoom on (d).

The OPD MTF which takes into account the effect of the QWLSI grating is different from the theoretical 3D MTF as described by Streibl [19]. For example, some frequencies close to the edge of the peanut shaped have a modulation which is upper than 1. These frequencies are responsible for the conical-shape of defocused SII OPD (see Fig. 8(b)) and are created by the barely visible shift of each unit interferogram formed by an unit illumination angle. There are also frequencies with negative v_z where the MTF vanishes inside the peanut-shaped structure (Figs. 7(d) and 7(e), brown medium-dashed curve).

The 3D MTF missing frequencies are observed experimentally on microbeads, with a nice butterfly-shape in Fig. 5(d): four lobes are clearly visible.

5. Experimental validation on calibrated samples

In the previous sections, we determined the value of the contrast loss on intensity and OPD images due the illumination incoherence. We experimentally compared the 3D spatial frequencies of images acquired with a QWLSI of model objects (microbeads) with those deduced from our simulation model (Fig. 5). The agreement is very good.

We now propose to use the calculated MTF to correct images of phase objects considering either projective hypothesis or 3D stacks. Two cases are studied: $5 \mu\text{m}$ beads (for quantitative value discussion) and 100 nm beads (i.e. below the diffraction limit for resolution purpose).

5.1. Quantitative measurement comparison

Let us first consider the study of polystyrene micro-beads. We use $5 \mu\text{m}$ beads (Sigma-Aldrich, St-Louis, USA) of theoretical refractive index $n=1.6$; the beads are deposited on a conventional cover slip, then immersed in an aqueous immersion medium (Cargille, Cedar Grove, USA) of

refractive index $n_{med} = 1.542$ measured with a commercial Abbe refractometer (2WAJ, HuiXia Supply, China), and finally sandwiched using another cover glass.

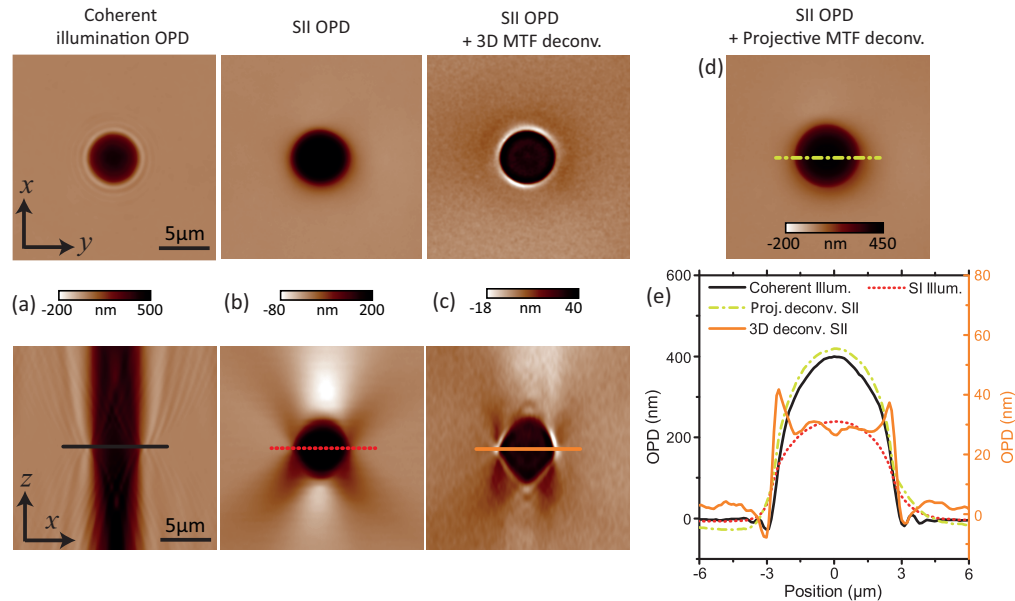


Fig. 8. OPD Z-stacks of a $5 \mu\text{m}$ polystyrene bead. Up: $z = 0$ plane. Down: $y = 0$ plane. (a) OPD measured with a quasi-plane-wave illumination. The Z-stack is obtained by numerical propagation. (b) OPD stack measured under SII with axial scanning of the objective. (c) Same as (b) plus deconvolution using the 3D MTF_{OPD} . (d) Same as (b) plus deconvolution of the $z = 0$ image (b).up using the projective MTF_{OPD} . (e) OPD line-outs along x by the center of the bead. Black curve: coherent illumination. Red dot curve: SI illumination. Yellow dashed dot curve: SII plus projective MTF_{OPD} . Orange curve: SII plus 3D MTF_{OPD} .

First, one bead is imaged under SII in different z planes by moving the objective with an axial step of 300 nm. We obtain a raw Z-stack of SII OPD using the QWLSI (Fig. 8(b)). Then, for comparison purpose, the EM field under coherent illumination is measured in the bead median plane. The spatial coherence is obtained by closing the Köhler aperture diaphragm to its minimum. An approximate refractive index value of $n_{coh} = 1.607 \pm 0.05$ can be extracted from the coherent OPD, considering that $OPD = t \times (n_{coh} - n_{med})$, where t is the local bead thickness deduced from its diameter in the OPD image [15]. The coherent EM field can be numerically propagated [1] to obtain a Z-stack (Fig. 8(a)).

As expected, the bead is much more resolved in the z axis on the raw SII OPD map (lower Fig. 8(b)) than in the coherent OPD stack (lower Fig. 8(a)). Also as expected, due to the frequency loss under incoherent illumination, a value decay is observed between the coherent measurement and the incoherent one : the maximum falls from 400 nm in the coherent OPD image (upper Fig. 8(a)) down to 240 nm in the raw SII OPD image (upper Fig. 8(b)). The lobes of the 3D MTF_{OPD} (Fig. 7(b)) explain the V-shape of the SII OPD along z and the asymmetry observed between positive and negative v_z of the 3D MTF_{OPD} explains why the map is non symmetrical about the $z = 0$ plane.

By a 2D deconvolution using the projective MTF_{OPD} (Fig. 6) one is able to compensate this contrast loss and retrieve OPD values now close to the coherent ones (Figs. 8(d) and 8(e)). It means that in focus SI 2D-deconvolved images can be interpreted in the same way as coherent OPD images (*i.e.* projective approximation).

By calculating first the Rytov 3D EM field and then deconvolving this 3D field using the 3D MTF_{OPD} (Fig. 7(b)), the artifacts on the defocused images (visible as a V-shape and white spots on the Fig. 8(b-down)) are strongly reduced (Fig. 8(c-down)). The ring visible around the bead after 3D deconvolution (Fig. 8(c-up)) is due to the non-collected frequencies (Fig. 4(b)). The remaining defocused artifacts may be explained, in particular their non-symmetric aspect, by the Gouy phase anomaly [39] that still exists with incoherent illumination.

The parabolic shape typical of the bead OPD visible on Fig. 8(e) for non-3D-deconvolved OPD images becomes more flat for 3D deconvolved images (Fig. 8(c-up)). The OPD values are also reduced compared to the coherent OPD (from 400 nm to 26 nm). It can be explained because this 3D deconvolved OPD corresponds to the OPD accumulated in each slice of the image. Indeed, when the 3D deconvolved OPD is summed along the optical axis, the resulting image is close to the 2D deconvolved image with a maximum OPD value of 450 nm in the center of the bead and a parabolic shape.

5.2. Resolution increase with SII

It is obvious when looking to the results on $5\ \mu\text{m}$ beads (Fig. 8(down)) that SII leads to a much higher axial sectioning compared to coherent illumination. For lateral resolution comparison we consider the study of $100\ \text{nm}$ TiO_2 beads immersed in water. These beads are non-resolved objects even under SII ($r_{x,y}^{SII} = 269\ \text{nm}$ at $\lambda = 700\ \text{nm}$) and can thus be considered as a point source.

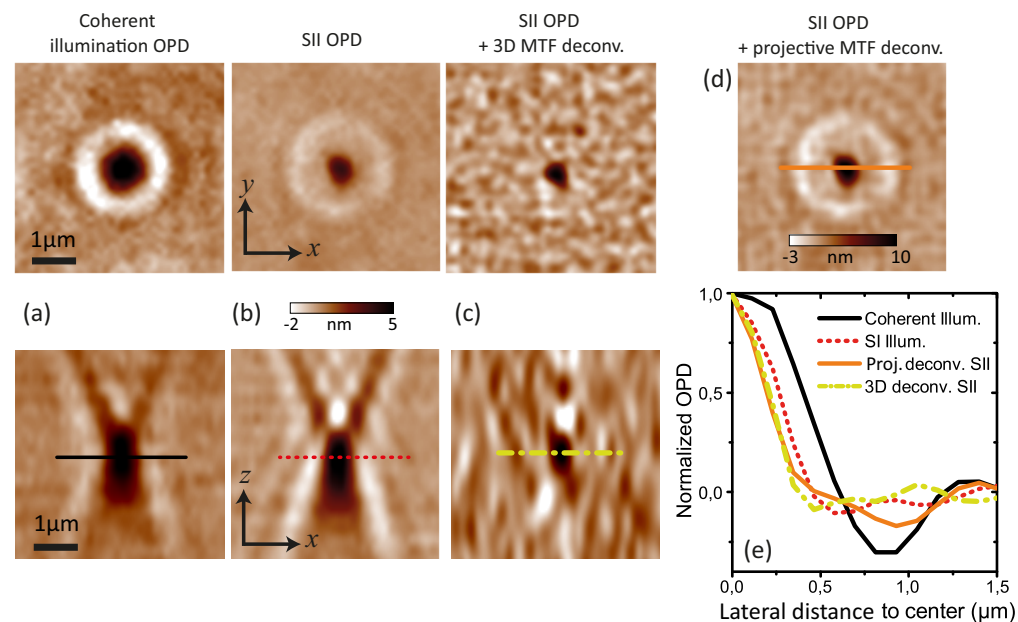


Fig. 9. OPD Z-stacks of a $100\ \text{nm}$ TiO_2 bead. Up: $z = 0$ plane. Down: $y = 0$ plane. (a) OPD measured with a quasi-plane-wave illumination. The Z-stack is obtained with axial scanning of the objective. (b) OPD stack measured under SII with axial scanning of the objective. (c) Same as (b) plus deconvolution using the 3D MTF_{OPD} . (d) Same as (b) plus deconvolution of the $z = 0$ image (b).up using the projective MTF_{OPD} . (e) OPD profile plots in the $z = 0$ plane of coherent OPD (black line), SII OPD (red dot line), 2D deconvolved SII OPD (orange line) and 3D deconvolved SII OPD (yellow dashed dot line). The resolution gain using SII is clearly visible.

Before deconvolution procedure, coherent (Fig. 9(a-bottom)) and incoherent illumination (Fig. 9(b-bottom)) axial OPD distributions are similar in first approach. The maximum axial frequency collected from this non-resolved structure is indeed the same for coherent and incoherent illumination (Fig. 4(b)). However, when using 3D deconvolution, the axial resolution is again improved with SII (Fig. 9(c-down)) compared to coherent illumination (Fig. 9(a-down)): the full-width at half-maximum of the OPD is equal to 1 μm for deconvolved SII stack compared to 2.4 μm for the coherent one.

For the lateral resolution (Fig. 9(e)), the point spread function is measured by radial averaging of the OPD images in the $z = 0$ plane. The theoretical PSF radius r_{PSF} is calculated using the equation:

$$r_{PSF} = 1.22 \frac{\lambda}{NA_{coll} + NA_{ill}}, \quad (16)$$

with $\lambda = 700$ nm, $NA_{coll} = 1.3$ and $NA_{ill} = 0$ for coherent illumination or $NA_{ill} = 1.3$ for totally SII. The results are summed up in the Table 5.2.

Table 1. Comparison between theoretical and experimental PSFs.

	Theo. PSF radius (nm)	Exp. measurements (nm)
Spatially coherent illum.	657	620 ± 30
SII	328	450 ± 30
SII + 2D deconv.	328	400 ± 30
SII + 3D deconv.	328	370 ± 30

As predicted, the lateral resolution is approximately increased by a factor 2 for 3D deconvolved SII OPD compared to spatially coherent illumination, the usual way to make QPI. The resolution is a little bit larger with SII than the theoretical one: this can be explained either by the optical aberration, or by the noise at very high spatial frequency which kills the useful information about the sample and thus cannot be retrieved by deconvolution. Moreover, a single 2D OPD measurement deconvolved with the theoretical projective MTF is not enough to completely remove the diffraction rings (Fig. 9(d)). A 3D MTF deconvolution on a stack of OPD images is required to get rid of the diffraction rings.

6. Conclusion

We demonstrated that single-shot quantitative phase imaging is possible even with incoherent illumination. This approach allows both lateral and axial resolution increase compared to the classical QPI under coherent illumination. Spatially incoherent illumination leads to much more resolution gain compared to polychromatic incoherent illumination. The lateral resolution with fully-SI trans-illumination scheme is the same as the one obtained using structured illumination holography [32, 33]. Thus, the 3D resolution is the same as for conventional fluorescence imaging.

However, SII also leads to spatial frequency dumping, characterized by the MTF. This dumping leads to non quantitative images and needs to be compensated. We propose a way to simulate the OPD MTF for any kind of illumination scheme. The particular case of projective MTF and 3D MTF are studied using our simulation tools. Moreover, the effect of the sensor (QWLSI) has also been taken into account to reconstruct the images.

As shown on polystyrene beads, a deconvolution of 2D SII OPD images using projective MTF leads to quantitative images that can be interpreted as if they were spatially coherent OPD images but with a doubled lateral resolution and a strong rejection of out-of-focus structures.

This approach will be useful for highly resolved dry-mass measurements [40] or anisotropy imaging [41]. For 3D SII OPD stacks, we consider Rytov EM field as a quantitative way to describe OPD variation in space. In this case, the OPD can be interpreted as if each slice was carrying the OPD accumulated through the depth-of-field. Moreover with 3D deconvolution, defocused OPD artifacts are reduced. This approach will be considered to obtain refractive index tomography and sample 3D structure imaging.

The resolution under SII is much better than under classical coherent illumination, with a gain close to 2 for lateral resolution. The axial resolution improvement using SII is particularly interesting when the sample is much larger than the depth-of-field, as the axial sectioning is very poor under coherent illumination.

With our deconvolved SII QPM technique, we will now consider thick biological sample imaging with the same 3D resolution as deconvolved fluorescence images. SII would be particularly useful when dealing with strongly scattering samples as the spatial coherence required for classical QPM may be lost through the sample. Experimental MTF determination will be studied to take into account the optical aberrations. We will also consider to achieve diffraction tomography in order to measure the local sample refractive index. This approach, using SII illumination and sample scanning, will speed-up and simplify the state-of-the-art way to do diffraction tomography (*i.e.* illumination angle scanning).

Acknowledgments

Financial support from the QuITO project funded by FUI and PACA Region is gratefully acknowledged. This work was also partially supported by ANR grant France Bio Imaging (ANR-10-INSB-04-01) and France Life Imaging (ANR-11-INSB-0006) Infrastructure networks.